Modelling of street-scale pollutant dispersion by coupled simulation of chemical reaction, aerosol dynamics, and CFD

Chao Lin [a,*,★], Yunyi Wang [b,★], Ryozo Ooka [c], Cédric Flageul [d], Youngseob Kim [b],

Hideki Kikumoto [c], Zhizhao Wang [b], Karine Sartelet [b]

[a] Graduate School of Engineering, The University of Tokyo, 4-6-1 Komaba, Meguro-ku, Tokyo 153-8505, Japan

[b] CEREA, École des Ponts ParisTech, EdF R&D, 77 455 Marne la Vallée, France

[c] Institute of Industrial Science, The University of Tokyo, 4-6-1 Komaba, Meguro-ku, Tokyo 153-8505, Japan

[d] Curiosity Group, Pprime Institute, Université de Poitiers, CNRS, ISAE-ENSMA, Chasseneuil, France

[*] Corresponding author, c-lin415@iis.u-tokyo.ac.jp

[★] These authors contributed equally to this work.

ABSTRACT

In the urban environment, gas and particles impose adverse impacts on pedestrians' health. The conventional computational fluid dynamics (CFD) methods that regard pollutant as passive scalar cannot reproduce the formation of secondary pollutants and lead to uncertain prediction. In this study, SSH-Aerosol, a modular box model that simulates the evolution of gas, primary and secondary aerosols, is coupled with the CFD softwares OpenFOAM and Code_Saturne. The transient dispersion of pollutants emitted from traffic in a street canyon is simulated using unsteady Reynolds-averaged Navier–Stokes equations (RANS) model. The simulated concentrations of NO_2, PM_{10} and black carbon are compared with field measurements on a street of Greater Paris. The simulated NO_2 and PM_{10} concentrations based on the coupled model achieved better agreement with measurement data than the conventional CFD simulation. Meanwhile, the black carbon concentration is underestimated, probably partly because of the underestimation of non-exhaust emissions (tyre and road wear). Aerosol dynamics lead to large increase of ammonium nitrate and anthropogenic organic compounds from precursor-gas emitted in the street canyon.

Keywords

Pollutant dispersion, Street canyon, Aerosol dynamics, CFD, PM_{10}, Secondary aerosols

1. Introduction

Traffic-related pollutants can impose adverse effects on pedestrians' health in the urban

37 environment (Anenberg et al., 2017; Jones et al., 2008). Especially, particulate matter
38 (PM) is strongly associated with increased cardiovascular diseases (Du et al., 2016).
39 Therefore, investigating the dispersion of PM and the corresponding precursor gas is of
40 great significance to evaluate the environmental impact and devise suitable
41 countermeasures (Kumar et al., 2008).

42 With the development of numerical simulations, computational fluid dynamics (CFD) has
43 been widely used for near-field dispersion prediction (Tominaga and Stathopoulos, 2013).
44 The pollutant dispersion patterns in complex geometric and non-uniform building
45 configurations can be well predicted using CFD simulations (Blocken et al., 2013).
46 Pollutant dispersion, deposition and transformation (chemical reactions and aerosol
47 dynamics) have primary roles in near-field prediction models. However, most CFD-based
48 studies assume that the time scale of transport at the street scale (~ 100 m) is relatively
49 shorter than the time scale of deposition and transformation; therefore, they frequently
50 regard pollutants as inert matter. Meanwhile, the recirculation flows which commonly
51 exist in street canyons lead to low-ventilation zones and may provide sufficient time for
52 transformation (Lo and Ngan, 2017; Zhang et al., 2020).

53 In addition, when PM is transported as a passive scalar, the distribution of the total
54 concentration can be simulated, however, information on the particle size distribution and
55 chemical composition is unclear. Understanding the size distribution is important for
56 evaluating the health hazards because large particles are deposited in the mouth and upper
57 airways, whereas smaller particles deposit deeper in the lungs and can even reach the
58 alveolar region of the lungs (Sung et al., 2007). In addition, as particles of different
59 chemical compositions are related to different sources and/or precursor gases, gaining
60 knowledge of their composition may help devise countermeasures to limit their
61 concentrations (Kim, 2019).

62 To simulate pollutant concentrations considering both transport and transformation, many
63 studies have coupled air-quality models with gas-phase chemistry and aerosol modules
64 and achieved chemical transport from a regional scale (~ 100 km) (Sartelet et al., 2007) to
65 a street scale (Lugon et al., 2021b). However, few models can simultaneously represent
66 detailed particle dispersion in a complicated urban flow field considering secondary
67 aerosol formation.

68 For the recent development and application of CFD-chemistry coupling model, Kurppa
69 et al., (2019) implemented a sectional aerosol module into large eddy simulation (LES),
70 and conducted a particle dispersion simulation on a neighborhood scale. Gao et al., (2022)
71 employed the same model to examine the dispersion of cooking-generated aerosols in an
72 urban street canyon. In both studies, the effect of particle dynamics on aerosol number

73 concentration was well reproduced. However, the simulated chemical composition was
74 not detailed. In addition, the chemical reactions of the precursor gas were not considered.
75 Kim et al., (2019) coupled unsteady Reynolds-averaged Navier-Stokes (RANS) model
76 with gas chemistry and aerosol modules and conducted simulations of PM_1 in a street
77 canyon under summer and winter conditions. The diurnal variations, spatial distribution
78 and chemical composition of pollutants in the street canyon were investigated. However,
79 the size distribution of particles and the secondary organic aerosol (SOA) chemistry were
80 not considered. Therefore, a more comprehensive coupled model is needed to simulate
81 the evolution of gas concentrations, mass and number concentrations of primary and
82 secondary particles at the same time.

83 Vehicles are considered to be the main ammonia (NH_3) source in urban environments
84 (Sun et al., 2017). Reactive nitrogen emissions from many new vehicles are now
85 dominated by NH_3 (Bishop and Stedman, 2015). Since the formation of ammonium
86 nitrate is often limited by HNO_3 rather than NH_3 in urban areas (NH_3-limited), increasing
87 NH_3 may lead to increased ammonium nitrate production and PM concentration in urban
88 streets (Lugon et al., 2021b). However, NH_3 emissions from passenger cars are usually
89 not regulated (Suarez-Bertoa and Astorga, 2018). Therefore, to provide evidence in
90 making policies for NH_3 emission regulation, it is important to investigate the local
91 influence of NH_3 emissions on PM concentrations.

92 Therefore, to achieve a more comprehensive simulation of PM and related precursor gas,
93 this study couple two open-source CFD softwares: OpenFOAM (OpenFOAM user guide)
94 and Code_Saturne (Archambeau et al., 2004), with gas-phase chemistry and aerosol
95 module SSH-Aerosol (Sartelet et al., 2020). Both OpenFOAM and Code_Saturne own
96 wide users. Therefore, coupling SSH-aerosol with both CFD softwares may satisfy more
97 needs. Simulations of the PM concentrations in a two-dimensional street canyon are
98 conducted. The coupled model is validated by comparison to field measurements. The
99 size distributions and chemical compositions of particles from the models with and
100 without secondary aerosol formation are compared. In addition, cases with large NH_3
101 emissions are considered and the related PM increase is investigated.

102 The remainder of this paper is organized as follows. The coupling of the aerosol model
103 and CFD is introduced in Section 2. The computational details are presented in Section 3.
104 In Section 4, the simulated pollutant concentrations are compared with field
105 measurements, followed by evaluations of the influence of the grid, coupling method and
106 time step. In Section 5, spatial and temporal variations in the concentrations are analyzed.
107 The chemical compositions and size distributions of the particles between the coupled
108 model and the model that does not consider gas chemistry or aerosol dynamics are

109   compared. In addition, the effect of NH_3 traffic emissions on particle concentrations is
110   discussed. Finally, the conclusions and perspectives are presented in Section 6.
111
112   **2. Model description**
113   The coupling method between CFD and chemistry modules is similar to the literature
114   (Gao et al., 2022; Kurppa et al., 2019). OpenFOAM v2012 and Code_Saturne 6.2 are
115   used to solve the governing equations of the flow field and transport equations of gas and
116   particle mass fractions. The inflow conditions, pollutants' background concentrations and
117   emission rates are obtained from regional models, and are linearly interpolated into each
118   time step, which will be introduced in Section 3. This simulation method is called
119   transient-condition method (TCM) in this study. However, because time-varying flow
120   fields and concentration fields are expensive to compute in terms of computational time,
121   conducting CFD simulations with fixed boundary conditions and emission rates at
122   specific time points is considered a practical method for evaluating street-level pollutant
123   concentrations (Wu et al., 2021; Zhang et al., 2020). The transport (advection and
124   diffusion) and chemical processes will reach equilibrium, and the simulated
125   concentrations will reach quasi-stable values. These values are often regarded as time-
126   averaged concentrations. This method is called the constant-condition method (CCM) in
127   this study, in contrast to TCM. However, the simulation accuracy of CCM has not been
128   validated in simulations that consider both gas chemistry and particle dynamics.
129   Therefore, validation is conducted using boundary conditions and emission rates at
130   specific time points and the simulated concentrations with CCM and TCM are compared
131   in Section 4.2.
132   The unsteady RANS model is used for the transient simulations with both CFD codes. In
133   OpenFOAM, the RNG (Re-Normalisation Group) k–ε model (Yakhot et al., 1992) is
134   deployed for turbulence closure. All transport equations are discretized using the total
135   variation diminishing (TVD) scheme (Harten, 1984; Yee, 1987), which combines the
136   first-order upwind difference scheme and the second-order central difference scheme. The
137   PIMPLE algorithm, a merged PISO (Pressure Implicit with Splitting of Operator)–
138   SIMPLE (Semi-Implicit Method for Pressure-Linked Equations) algorithm in the
139   OpenFOAM toolkit, is used for pressure–velocity coupling. In Code_Saturne, turbulence
140   is solved using the k–ε turbulence model (linear production) (Guimet and Laurence, 2002).
141   The time and space discretizations of velocity, pressure and other scalars in all transport
142   equations are realized through a centred scheme and a fractional step scheme
143   (Archambeau et al., 2004) . For both CFD software, the dry deposition schemes for gas
144   and particle are added to the transport equations using volume sink terms based on Zhang

145 et al. (2003) and Zhang et al. (2001), respectively. The details of the implementation are

146 provided in Appendix A.

147 SSH-Aerosol (Sartelet et al., 2020) is a modular box model that simulates the evolution

148 of not only gas concentrations but also the mass and number concentrations of primary

149 and secondary particles. In SSH-Aerosol 112 gas species and 40 particle species are

150 considered. The particle compounds are dust, black carbon, inorganics (sodium, sulphate,

151 ammonium, nitrate and chloride), primary organic aerosol (POA) and secondary organic

152 aerosol (SOA). Three main processes involved in aerosol dynamics (coagulation,

153 condensation /evaporation and nucleation) are included. The particle size distribution is

154 modelled using a sectional size distribution. Nucleation is not considered in this study

155 because only the mass and not the number of particles is available for evaluation, and

156 large uncertainties remain on the nucleation parameterizations (Sartelet et al., 2022)

157 mostly affecting the number of particles. As nucleation is not considered, the minimum

158 diameter does not need to be as low as 0.001 μm, and it is fixed to 0.01 μm, as in the

159 regional-scale simulations of Sartelet et al. (2018), which provide the background

160 concentrations. Six particle size sections are employed with bound diameters of 0.01, 0.04,

161 0.16, 0.4, 1.0, 2.5 and 10 μm.

162 The coupling between CFD and SSH-aerosol are achieved by using the application

163 program interface (API) of SSH-aerosol. The gas and particle concentrations are

164 initialized in CFD and are transported in the domain for each time step. For each grid

165 volume cell, these transported concentrations, as well as meteorological parameters, such

166 as temperature and humidity, are then sent to SSH-aerosol to advance one time step of

167 gaseous chemistry and aerosol dynamics. Once the SSH-aerosol calculation is completed,

168 the concentrations are sent back to the CFD for the next time step. It should be noted that

169 as the SSH-aerosol processes the ensemble-averaged concentration from RANS model,

170 the covariance of turbulent diffusion and chemical reaction may not be fully reproduced.

171 The influence of different operator splitting algorithms is discussed in Section 4.4.

172

173   **3. Simulation setup**
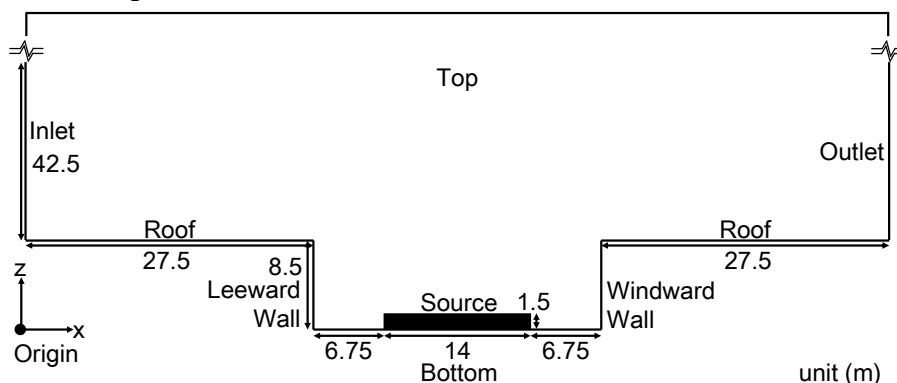
174

175   Fig. 1 Simulation domain of street canyon

176

177   The simulation is set up to model a street in Greater Paris (Boulevard Alsace-Lorraine),
178   where field measurements were conducted from April 6 to June 15, 2014. The
179   concentrations of nitrogen dioxide (NO_2), particles with diameters less than 10 μm (PM_{10}),
180   and black carbon were measured as described in (Kim et al., 2018). Fig. 1 shows the
181   simulation domain. The 2-D street canyon is 27.5 m in width (W) and 8.5 m in height
182   (H). The domain height is 6 H. The street canyon is discretized into uniform grids in x-
183   and z- directions. The grid resolutions in the street canyon are 0.5 m in both x-and z-
184   directions, respectively. The largest grid sizes are 4 m (x) × 2m (z). An analysis of the
185   grid sensitivity is described in Section 4.3.
186   Simulations are conducted from 4:30 a.m. to 5 p.m. on April 30, 2014 at local time
187   (GMT+2). This period is selected because the wind direction is almost perpendicular to
188   the street canyon during that day, allowing for a 2D simulation setting. During the field
189   measurement, there exists several time periods that the wind direction is perpendicular
190   with the street canyon. Meanwhile, some time periods are short (less than 5 hours), and
191   we consider that short period simulation is not representative in simulation accuracy. In
192   addition, we consider that it is critical to have a simulation time long enough to cover
193   both day-time chemistry and night-time chemistry. The first 30 minutes of the simulation
194   corresponds to model spin-up, and the simulation lasts 12 hours. A sensitivity analysis of
195   numerical aspects, such as the splitting method between transport and chemistry and the
196   time step, is described in Section 4.4.

197
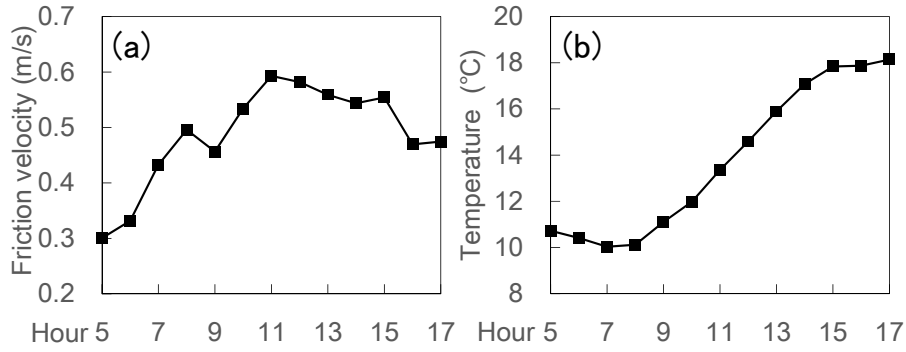
198 Fig. 2 Time variations of hourly friction velocity and temperature for inflow.

199

200 Meteorological conditions (Fig. 2) including time-varying friction velocity and
201 temperature are obtained from the simulation described in Sartelet et al. (2018) using the
202 Weather Research and Forecasting (WRF) model. The grid resolution is 1 km ×1 km in
203 Paris. The lowest and highest friction velocities occurred approximately at 5 a.m. and 11
204 a.m., respectively. The lowest and highest temperatures are around 8 a.m. and 5 p.m. For
205 the inflow, the wind direction is perpendicular to the street canyon. The friction velocity
206 u_* is used to prescribe the vertical profiles of the streamwise velocity U, turbulent kinetic
207 energy k and turbulent dissipation rate ε as follows

$$U(z) = \frac{u_*}{\kappa} \ln\left(\frac{z - H}{z_0}\right) \tag{1}$$

$$k(z) = \frac{u_*^2}{\sqrt{C_\mu}} \tag{2}$$

$$\varepsilon(z) = \frac{u_*^3}{\kappa(z - H)} \tag{3}$$

208 where κ is the von Kármán constant and C_μ is the model constant (=0.09) in the k-ε
209 model. The roughness length z_0 is set to 1 m for the inlet (Belcher, 2005) and 0.1 m for
210 the wall and bottom (Lo and Ngan, 2015).
211 In addition, since the domain height is low (51 m) in this study and we focus on the
212 pollutant dispersion behaviors in the street canyon, it is reasonable to consider the
213 atmospheric stability as neutral; therefore the temperature is assumed to be spatially
214 uniform at the inflow. The hourly friction velocities and temperatures are linearly
215 interpolated into each timestep and prescribed at the inflow. It should be noted that the
216 general trends are simulated but the fast fluctuations at the inlet are not reproduced. The
217 same linear interpolation is used for background concentrations and emission rates, which
218 will be described in the following.

219
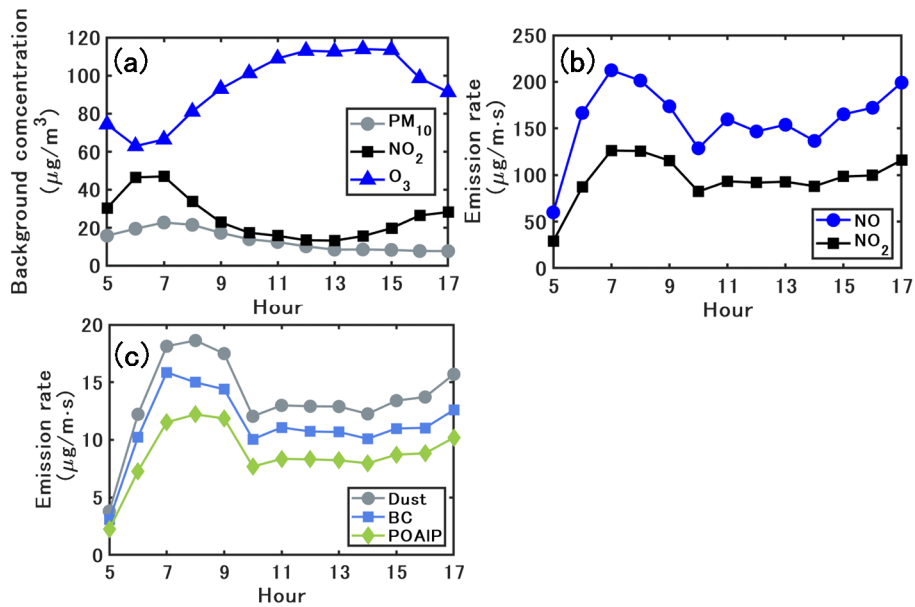
221 Fig. 3 Time variations of (a) PM_{10}, NO and NO_2 background concentrations, (b) emission
222 rates of NO and NO_2 and (c) emission rates of dust, BC and organics (POAlP).

224 Fig. 3(a) shows the time variations of the PM_{10}, NO and NO_2 background concentrations.
225 Fig. 3(b) and (c) show the emission rates for NO, NO_2 and the emitted compounds of
226 PM_{10}. The background concentrations of the gas and particles are obtained from the
227 regional-scale simulations of Sartelet et al. (2018) with the Eulerian model Polair3D of
228 the Polyphemus air quality modelling platform (Mallet et al., 2007), which uses the same
229 chemical representation as in this study. As detailed in Sartelet et al. (2018), the regional
230 background concentrations compare well to measurements of O_3, NO_2, PM_{10}, $PM_{2.5}$,
231 black carbon and organic aerosols. The hourly background concentrations are linearly
232 interpolated into each timestep and spatial-uniformly prescribed at the inflow and top.
233 The traffic emission source is assumed to be approximately 14 m in width and 1.5 m in
234 height, and it is set in the middle of the bottom of the canyon (Fig. 1). As detailed in Kim
235 et al. (2022), emissions are estimated from the fleet composition and the number of
236 vehicles in the street using COPERT's emission factors (COmputer Program to calculate
237 Emissions from Road Transport, version 2019, EMEP/EEA, 2019). After the speciation
238 of NO_x, Volatile Organic Compounds (VOC), $PM_{2.5}$ and PM_{10} into model species,
239 emissions are set for 16 gaseous model species and three particle model species: dust and
240 unspecified matter (Dust), black carbon (BC) and primary organic aerosol of low
241 volatility (POAlP). The PM size distribution at emission is assumed to be the same as in
242 the previous studies (Lugon et al., 2021a, 2021b). The exhaust primary PM is assumed to
243 be in the size bin [0.04 – 0.16 μm] while non-exhaust primary PM is coarser in the size

244   bin [0.4 – 10 μm].

245   For the boundary conditions of the OpenFOAM, the pressure and the gradients of all other

246   variables are set to zero at the outlet. For the walls, we use the wall functions of ε and

247   turbulent kinematic viscosity ν_t for atmospheric boundary layer modelling in

248   OpenFOAM toolkit (OpenFOAM user guide) based on (Parente et al., 2011). The

249   gradients of turbulent kinetic energy k, concentration, and temperature are set to zero. In

250   Code_Saturne, a two-scales logarithmic friction velocity wall function is used for solving

251   the fluid velocity near wall cell and a three layers wall function is used for computing

252   other transported scalar profiles such as temperature near the wall (Arpaci and Larsen,

253   1984).

254   The turbulent Schmidt number Sc_t in the concentration transport equations, which is the

255   ratio of the turbulent diffusivity to the concentration and turbulent kinematic viscosity, is

256   important in turbulent diffusion modeling. The value of Sc_t is considered between 0.2

257   and 1.3, depending on the flow properties and geometries (Tominaga and Stathopoulos,

258   2007). For urban environments with a compact layout, a small $Sc_t = 0.4$ is found to

259   show better agreement with wind tunnel experiment data (Di Sabatino et al., 2007).

260   Therefore, a value of 0.4 is adopted in the current study.

261

262   **4. Model evaluation**

263   *4.1. Validation with field measurements and comparison of simulated concentrations with*

264   *the two CFD software*
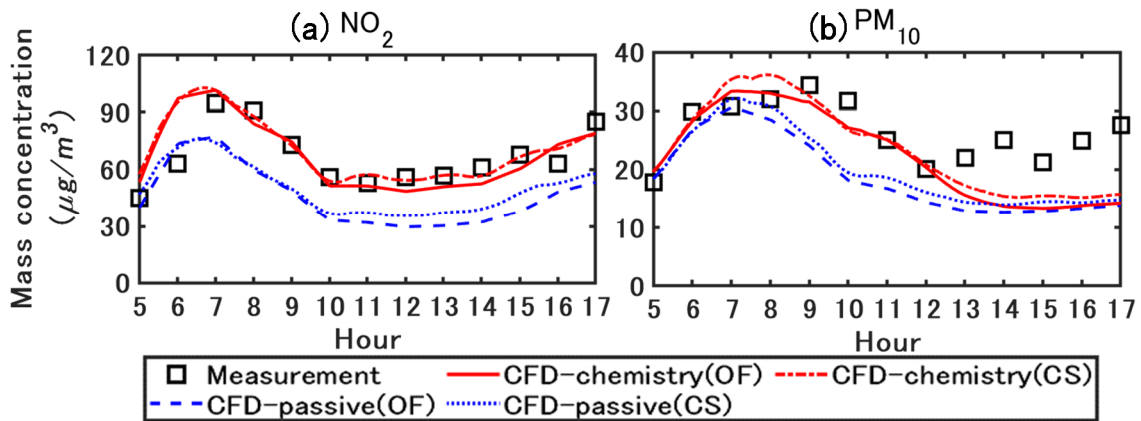
265   Fig. 4 Measured and simulated NO_2 and PM_{10} concentrations. The values are spatially

266 averaged in the street canyon ($27.5 \leq x \leq 55, 0 \leq z \leq 8.5$ m). CFD-passive and CFD-

267 chemistry denote the CFD simulation without and with chemistry coupling. OF and CS

268 denote the simulated concentrations based on OpenFOAM and Code_Saturne. All

269 concentrations are represented in local time (GMT+2).

270

271

272 Reproducing the flow field is important in this study. Meanwhile, the observation data on
273 wind velocity is not available. Therefore, we conducted a velocity validation for
274 OpenFOAM v2012 using data from a wind tunnel experiment (Blackman et al., 2015).
275 The predicted mean velocity agreed well with the experimental values. The details can be
276 found at Appendix B.

277 Fig. 4 compares the simulated concentrations with those obtained from the field
278 measurements. In the field measurements, the measured concentration was obtained from
279 averaging over two measurement points near the leeward and windward walls in the street
280 canyon. In this section, the simulated results and discussion are based on the spatially-
281 averaged values in the street canyon ($27.5 \leq x \leq 55, 0 \leq z \leq 8.5$ m). CFD-passive and
282 CFD-chemistry denote the CFD simulation without and with chemistry coupling. OF and
283 CS denote simulated concentrations based on OpenFOAM and Code_Saturne. The
284 operator splitting order and time step for OF and CS are the A-B-A splitting method with
285 0.5 s and the A-B splitting method with 0.25 s, as detailed in Section 4.4. The simulation
286 time ratio of CFD-chemistry and CFD-passive is about three times in both OpenFOAM
287 and Code_Saturne in this study.

288 For NO_2, the peak concentration in the field measurement occurred approximately at 7
289 a.m. owing to the morning traffic. In the CFD-passive simulations, the lack of chemical
290 reactions lead to an underestimation of NO_2, while the concentrations simulated with
291 CFD-chemistry agree well with the measurements. For PM_{10}, the concentrations
292 simulated with CFD-chemistry also show better agreement with the measurements than
293 CFD-passive. The primary reason is that CFD-chemistry can reproduce the condensation
294 of inorganic and organic matter from the gas phase to the particle phase, which will be
295 further explained in the following sections. The simulation results based on OF and CS
296 show small differences, and detailed comparisons are presented in Fig. 6.

297 Validation metrics (Chang and Hanna, 2004) are used to quantify the overall accuracy of
298 the CFD simulated concentrations based on OF, compared with the measured values
299 (Trini Castelli et al., 2018; Ferrero et al., 2019). The following metrics are used: fractional
300 bias (FB), geometric mean bias (MG) and normalized mean square error (NMSE). These
301 metrics are defined as follows:

$$\text{FB} = \frac{\overline{Obs} - \overline{CFD}}{0.5\left(\overline{Obs} + \overline{CFD}\right)} \tag{4}$$

$$\text{MG} = \exp\left(\overline{\ln Obs} - \overline{\ln CFD}\right) \tag{5}$$

$$\text{NMSE} = \frac{\overline{(Obs_i - CFD_i)^2}}{\overline{Obs} \times \overline{CFD}} \tag{6}$$

302 where Obs_i and CFD_i are the measured and CFD simulated concentrations for the

303   compound/species i, respectively. The overbar represents the mean value of the entire

304   dataset. The ideal values are 1 for MG, and 0 for FB and NMSE. Previous research has

305   suggested that $|FB| < 0.3,\ 0.7 < MG < 1.3$ and NMSE < 4 are acceptable for

306   simulated concentrations (Hanna et al., 2004).

307   Table 1 shows the statistical indicators for spatially averaged concentrations of NO_2 and

308   PM_{10} in the street canyon from 5 a.m. to 5 p.m. For NO_2 and PM_{10}, the mean and 90%

309   percentile concentrations simulated with CFD-chemistry are closer to the measurements

310   than those simulated with CFD-passive. In addition, the FB, MG and NMSE values of

311   CFD-chemistry are closer to the ideal values than those of CFD-passive.

312

313   Table 1 Statistical indicators for NO_2 and PM_{10} in the street canyon from 5 a.m. to 5p.m.

314   The concentrations are simulated with OpenFOAM.

	Concentration (µg/m³)		Validation metrics		
NO_2	Mean	Percentile 90%	FB	MG	NMSE
Measurement	66.6	91.8	/	/	/
CFD-chemistry	67.3	97.3	-0.01	1.00	1E-4
CFD-passive	45.9	73.7	0.36	1.50	0.14
PM_{10}	Mean	Percentile 90%	FB	MG	NMSE
Measurement	26.4	32.5	/	/	/
CFD-chemistry	22.3	33.1	0.17	1.23	0.03
CFD-passive	18.8	28.9	0.34	1.45	0.13

315
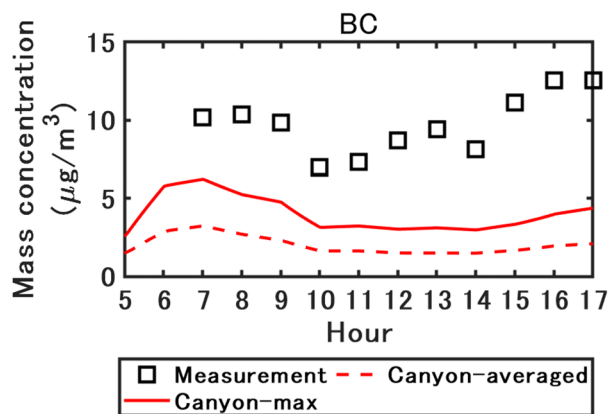
316

317   Fig. 5 Measured and simulated black carbon concentrations with OpenFOAM. The

318   canyon-averaged and maximum concentrations in the street canyon are represented by

319   the plain line and the dashed line respectively ($27.5 \leq x \leq 55, 0 \leq z \leq 8.5$ m).

320

321 The black carbon (BC) concentration simulated with OF is compared with the
322 measurements in Fig. 5. Because BC is considered an inert matter, considering chemistry
323 does not influence the mass concentration. Therefore, the concentrations simulated with
324 CFD-passive and CFD-chemistry show little difference; only the concentration simulated
325 with CFD-chemistry is shown here. The BC concentrations are underestimated by a factor
326 of approximately 5. Even the maximum concentrations in the street canyon largely
327 underestimate the measurements. One of the causes of this underestimation may be the
328 underestimation of the non-exhaust tyre emission factors in the COPERT emission factors
329 used here (Lugon et al., 2021a).
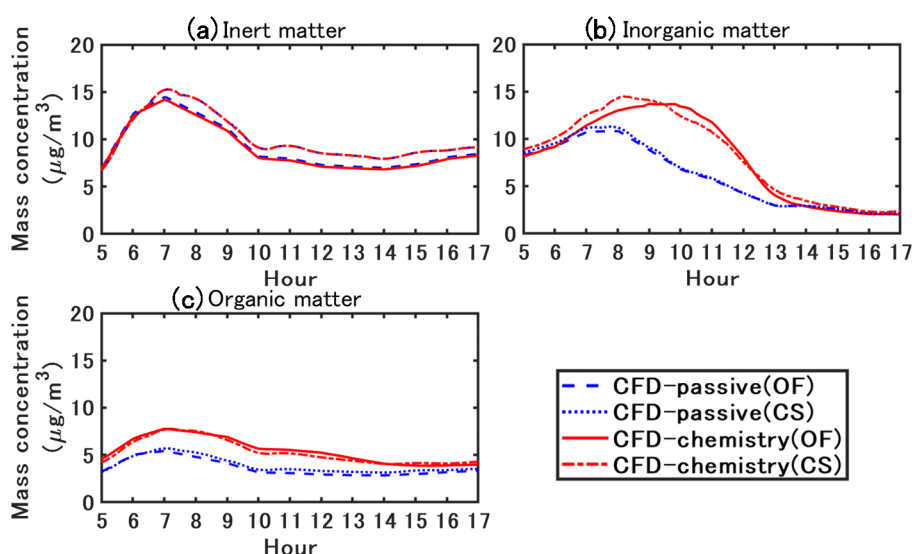
330
331 Fig. 6 Simulated particle concentrations with OpenFOAM (OF) and Code_Saturne (CS).
332 CFD-passive and CFD-chemistry denote the CFD simulation without and with chemistry
333 coupling.
334
335 The particle concentrations simulated with OF and CS are compared in Fig. 6. The
336 evolutions of the concentrations simulated by OF and CS are similar. Higher PM_{10}
337 concentrations are simulated by CS around 8 a.m. during the traffic peak and in the
338 afternoon, mostly because of the higher concentrations of emitted inert compounds, such
339 as black carbon and dust. Differences in the turbulence scheme may explain these
340 variations. Meanwhile, the difference between CFD-passive and CFD-chemistry for the
341 inorganic and organic matter is in accordance with OF and CS, showing the robustness
342 of the coupling method between CFD and SSH-aerosol by API. For simplicity, only the
343 simulated concentration based on OF is presented and discussed in the following sections.
344

345   *4.2. Transient-condition method and constant-condition method*
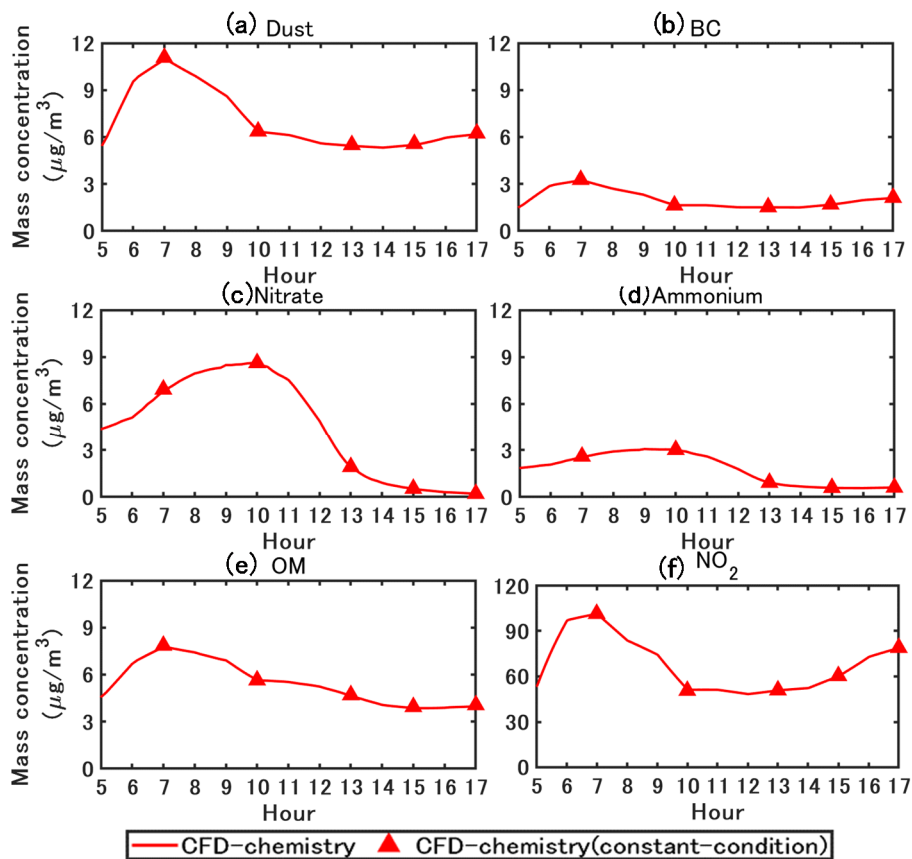
346

347   Fig. 7 Simulated PM_{10} and NO_2 concentrations with the transient-condition and constant-

348   condition methods. The concentrations are spatially averaged in the street canyon.

349

350   To validate the simulation accuracy of CCM in simulations that consider both gas

351   chemistry and particle dynamics, simulations are conducted using boundary conditions

352   and emission rates at five time points (7 a.m., 10 a.m., 1 p.m., 3 p.m. and 5 p.m.). Other

353   simulation conditions, including the grid, coupling method, and time step, are the same

354   as the transient-condition simulation.

355   In Fig. 7, for PM_{10} and NO_2, the concentrations simulated with CCM (red triangles) are

356   similar to those simulated with TCM. In addition, depending on the background

357   concentration and emission conditions, the simulation time required for CCM to reach

358   dynamic equilibrium is less than 1000 time steps (approximately 500 s). Therefore, CCM

359   can be utilized for parameter studies. The sensitivity analysis of the grid, coupling method

360   and time step in Section 4.3 and 4.4 is based on CCM. However, CCM should be used

361   with caution when the inflow wind speed and direction vary rapidly. The simulated

362   concentrations in Section 5 are based on TCM.

363

364   *4.3. Grid sensitivity*
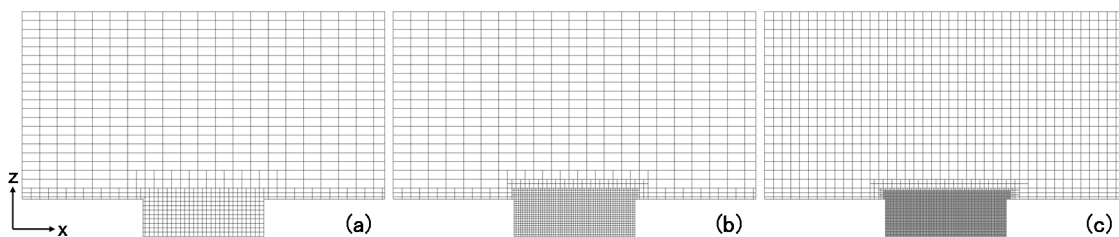
365

366   Fig. 8 Different grid resolutions for sensitivity analysis: (a) coarse, (b) basic, (c) fine. The
367   grid resolutions in the street canyon are 1 m, 0.5 m and 0.25 m in both *x*-and *z*- directions,
368   respectively. The largest grid sizes are 4 m (x) × 2m (z) in the coarse and basic grids,
369   and 2 m (x) × 2m (z) in the fine grid.
370

371   Grid sensitivity analysis is conducted based on three different resolutions as shown in Fig.
372   8. The grid resolutions in the street canyon for coarse, basic and fine grids are 1 m, 0.5 m
373   and 0.25 m in both *x*-and *z*- directions, respectively. The largest grid sizes are 4 m (x) ×
374   2m (z) for the coarse and basic grids, and 2 m (x) × 2m (z) for the fine grid. The
375   simulations are based on constant-condition method. The A-B-A splitting method, which
376   is introduced in Section 4.4, is used with a time step of 0.5 s. Fig. 9 shows the comparative
377   results for the mass concentration. No significant discrepancy is observed between the
378   different grids for NO_2, inert matter and organic matter. Meanwhile, the simulated
379   inorganic matter based on coarse grids shows slightly smaller concentrations than the
380   other grid resolutions, while the concentrations based on basic and fine grids are close.
381   Therefore, the basic grid is adopted for simulations in this study.
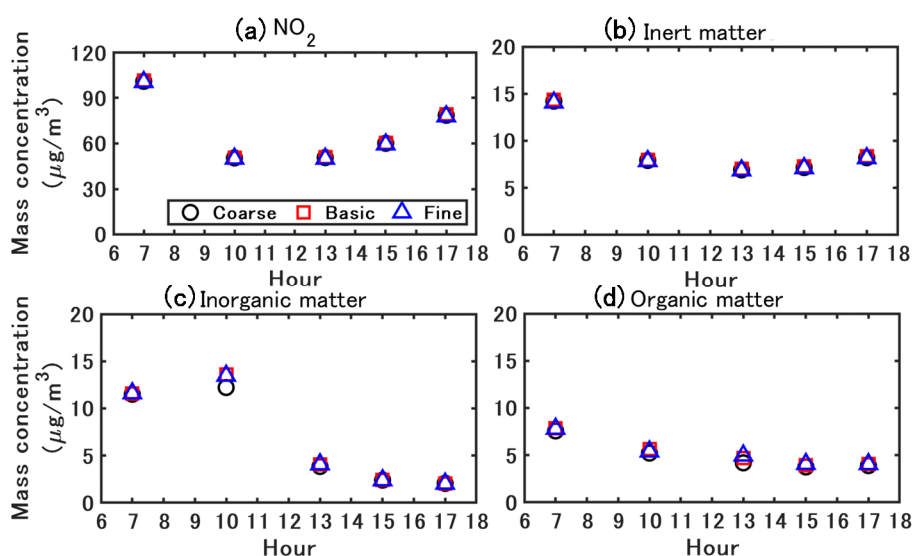
382

383   Fig. 9 Simulated NO_2 and particle concentrations with different grid resolutions.

384

385 *4.4. Coupling method and time step sensitivity*

386 The transport equation for the chemical species includes terms of advection, diffusion,

387 emission and chemical reactions. Ideally, the transport equation should be solved with all

388 the above terms, that is, by coupling all processes. However, the chemical process is

389 integrated with a stiff integrator, whereas advection, diffusion and emission are integrated

390 with a flux scheme. Therefore, operator splitting (Sportisse, 2000) is often employed to

391 solve different terms individually and sequentially over a given time step in chemical

392 transport simulations (Fu and Liang, 2016).

393 In this study, advection, diffusion and emission are simultaneously solved in CFD, and

394 the chemical reactions including gas chemistry, particle dynamics and size redistribution

395 are solved in SSH-Aerosol. Two operator-splitting orders are considered for coupling: A-

396 B splitting and A-B-A splitting (Sportisse, 2000). For A-B splitting, which can be

397 summarized as CFD(Δt)-Chemistry(Δt), the mass concentrations are first integrated for

398 transport over a time step Δt. The updated concentrations are then integrated for

399 chemistry at the same Δt. On the other side, A-B-A splitting adopts a symmetric sequence

400 of operators, which can be summarized as CFD($\Delta t/2$)-Chemistry(Δt)-CFD($\Delta t/2$). The

401 mass concentrations are first integrated for transport over a half time step, then for

402 chemistry over the full time step and finally for transport again over a half time step.

403

404 Table 2 Relative change in the computation time with different operator-splitting order

405 and time steps. The computation time is normalized by ABA-05.

Case	Operator splitting order	Δt (s)	Change in the computation time
AB-05	A-B splitting CFD(Δt)-Chemistry(Δt)	0.5	0.90
AB-025		0.25	1.56
ABA-1	A-B-A splitting CFD($\Delta t/2$)-Chemistry(Δt)-CFD($\Delta t/2$)	1	0.57
ABA-05		0.5	1
ABA-025		0.25	2.44

406

407 A sensitivity analysis is conducted on the operator splitting method and splitting time step.

408 As shown in Table 2, the time step is considered 0.5 s and 0.25 s for the A-B splitting

409 (named AB-05 and AB-025), and 1 s, 0.5 s and 0.25 s for the A-B-A splitting (named

410 ABA-1, ABA-05 and ABA-025). The simulated NO_2 and particle concentrations are

411 presented in Fig. 10. ABA-1 and AB-05 concentrations hardly differ from the figures.

412 Meanwhile, the computational time of ABA-1 is only 63% of that of AB-05. Similarly,

413 the concentrations simulated with ABA-05 and AB-025 are almost the same, and the

 computational time of ABA-05 is only 64% of AB-025. Therefore, the A-B-A splitting

415   method can be considered as a cost effective method.

416
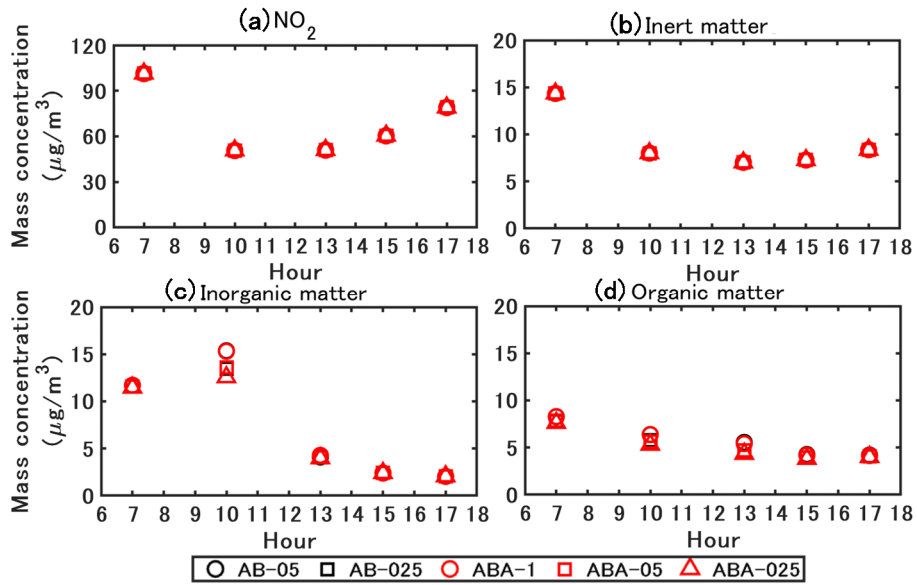
417

418   Fig. 10 Simulated NO_2 and particle concentrations with different coupling methods and

419   time steps. ABA denotes the A-B-A splitting method: CFD(Δt/2)-Chemistry(Δt)-

420   CFD(Δt/2). AB denotes the A-B splitting method: CFD(Δt)-Chemistry(Δt). In the legend,

421   the values that follow the capital letter ABA or AB denote the time step Δt (in s) used in

422   the simulation.

423

424   The concentrations simulated with the A-B-A splitting method and different time steps

425   show that small time step results in low inorganic and organic matter concentrations. The

426   concentrations simulated with ABA-1 are larger than those of ABA-05, and larger than

427   ABA-025. However, the differences between the concentrations simulated with ABA-05

428   and ABA-025 are lower than the differences between ABA-1 and ABA-05. For NO_2 and

429   inert particles, no obvious difference is found between the simulations with different

430   splitting methods and splitting time steps. Therefore, the A-B-A splitting method with a

431   time step of 0.5 s is adopted in this study.

432

5. Results and discussion

5.1. Time-averaged flow field and concentration field
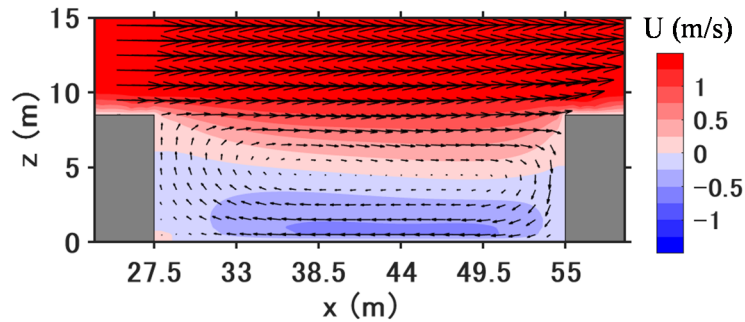
Fig. 11 Time-averaged flow field in the street canyon from 5 a.m. to 5 p.m.

This section shows the results for time-averaged values from 5 a.m. to 5 p.m. Fig. 11 shows the 12-hour time-averaged streamwise velocity and wind direction in the street canyon. At the current aspect ratio (*H*/*W*=0.31), a large vortex is observed in the canyon with a small secondary vortex at the corner of the leeward wall. A reverse flow is observed in the lower half of the canyon.
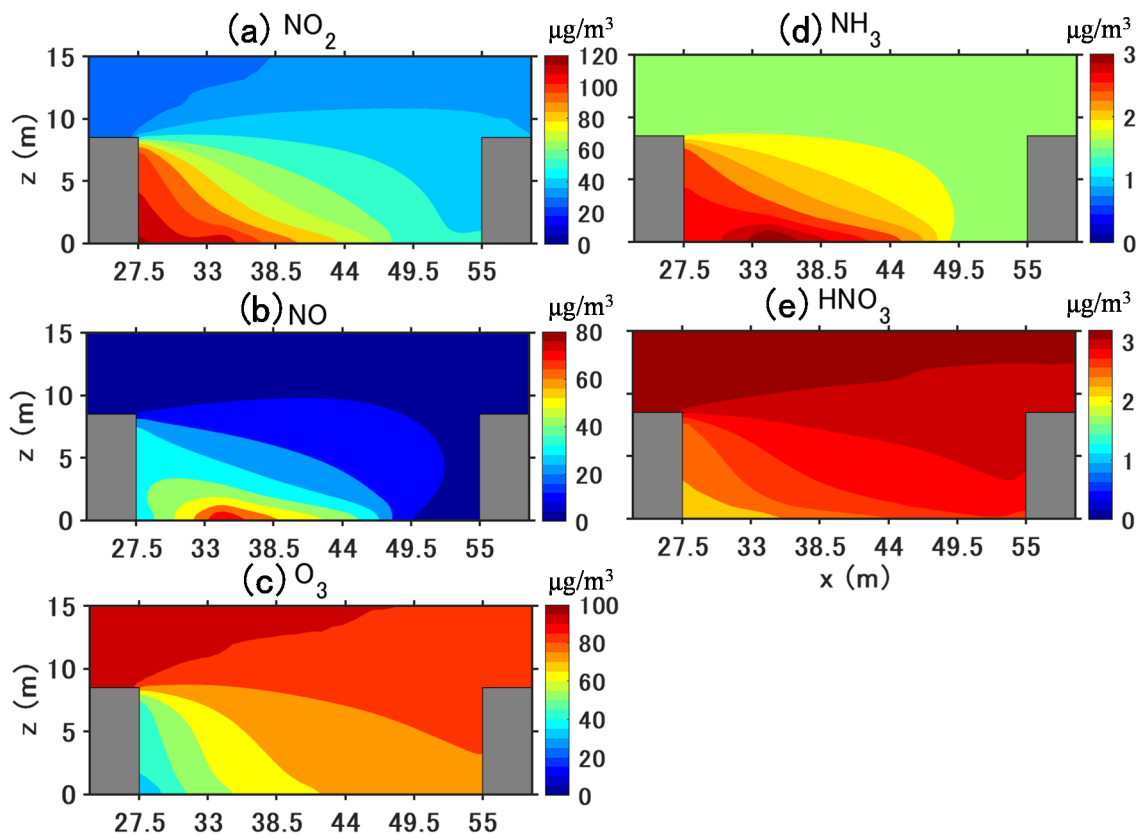
Fig. 12 Time-averaged concentrations ($\mu g/m^3$) of gaseous pollutants in the street canyon

445   from 5 a.m. to 5 p.m.

446

447   Fig. 12 shows the time-averaged concentrations of the gaseous pollutants from 5 a.m. to
448   5 p.m. For gaseous pollutants emitted by traffic, such as NO_2, NO and NH_3, larger
449   concentrations are found in the street, particularly near the leeward wall, compared to the
450   windward wall due to the reverse flow. Simultaneously, gas-phase chemistry and
451   condensation/evaporation between the gas and particle phases also influence the
452   concentration distribution. NO_2 mainly increases due to chemical production from NO
453   emissions and background O_3. Compared to the background NO_2 concentration of 26
454     $\mu g/m^3$, the longest retention time at the leeward side corner leads to the street canyon's
455   largest concentration (121 $\mu g/m^3$). At pedestrian height (z=1.5 m), NO_2 concentration is
456   116 $\mu g/m^3$ at the leeward wall and 49 $\mu g/m^3$ at the windward wall.
457   However, NO and NH_3 generally decrease because of loss by gaseous chemistry and the
458   condensation of ammonium nitrate, respectively; therefore, the largest concentrations are
459   at the leeward corner of the traffic emission source. For secondary gaseous pollutants
460   without traffic emissions such as O_3 and HNO_3, gaseous chemistry and condensation lead
461   to lower concentrations in the street canyon than background concentrations. For O_3, this
462   is due to the titration of O_3 by NO, whose concentration is large near the leeward wall.
463   For HNO_3, this is because of the high concentrations of NH_3, which then condenses with
464   HNO_3 to form ammonium nitrate. In addition, the lowest concentration of O_3 and HNO_3
465   can be found at the leeward corner which corresponds to the secondary vortex in Fig. 11,
466   indicating that the pollutant residence time is the highest in that corner leading to enhance
467   ozone titration.
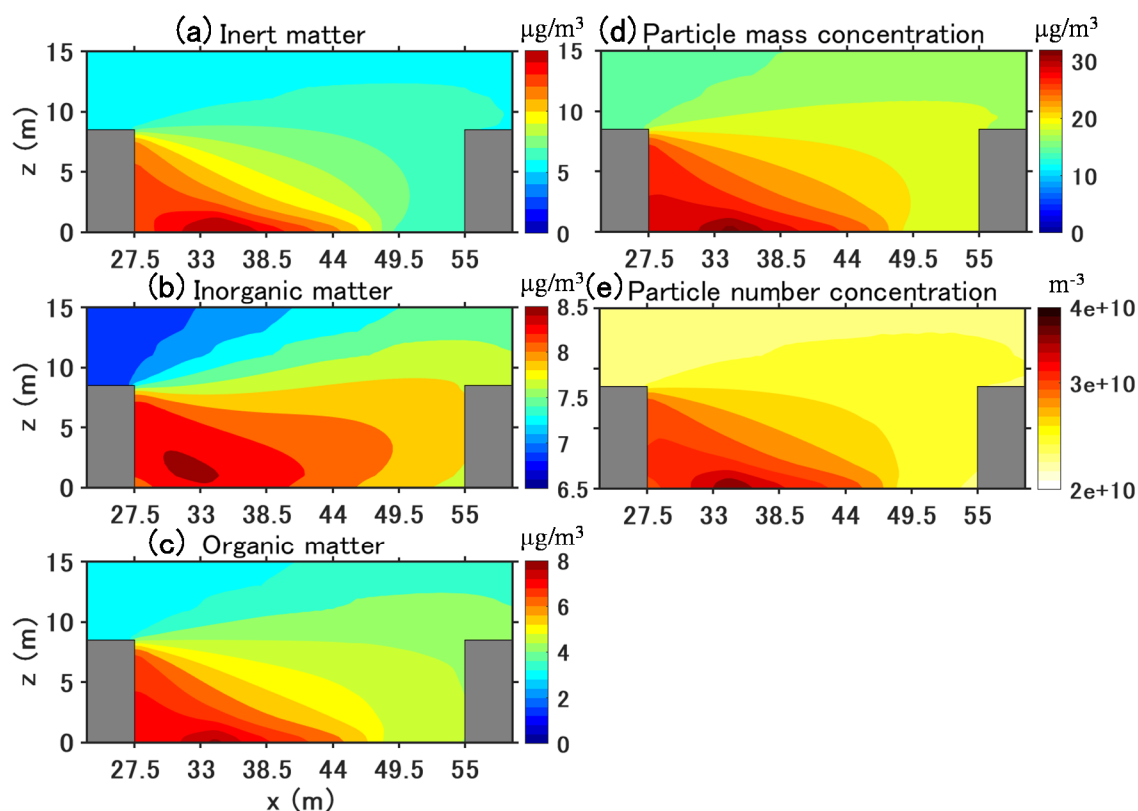
Fig. 13 Time-averaged concentrations of particle number, mass and composition in the street canyon from 5 a.m. to 5 p.m. The unit is $\mu g/m^3$ for mass concentration and m^{-3} for number concentration.

Fig. 13 shows the time-averaged PM_{10} mass concentration, and the number concentrations and PM composition (inorganic, organic and inert matter) from 5 a.m. to 5 p.m. For inert and organic matter, the highest concentrations are near the leeward corner of the traffic emission source. Because inorganic matter is not emitted, the concentration distribution differs from inert and organic matter. However, as they are produced from gas condensation and strongly influenced by traffic emissions, the highest concentrations are observed in the leeward corner.

At pedestrian height (z=1.5 m), the PM_{10} mass concentration is approximately 28 $\mu g/m^3$ at the leeward wall and 19 $\mu g/m^3$ at the windward wall, which is larger than the background concentration of 15 $\mu g/m^3$. The number concentration is computed from the mass concentration and therefore has a similar spatial distribution as PM_{10} mass concentration (nucleation from gas was not taken into account). Traffic emission significantly increases the number concentration. The number concentration is about 2.3×10^{10} m^{-3} in the background, whereas the largest number concentration in the street canyon is about 3.8×10^{10} m^{-3}.

488

5.2. Time-variant characteristics
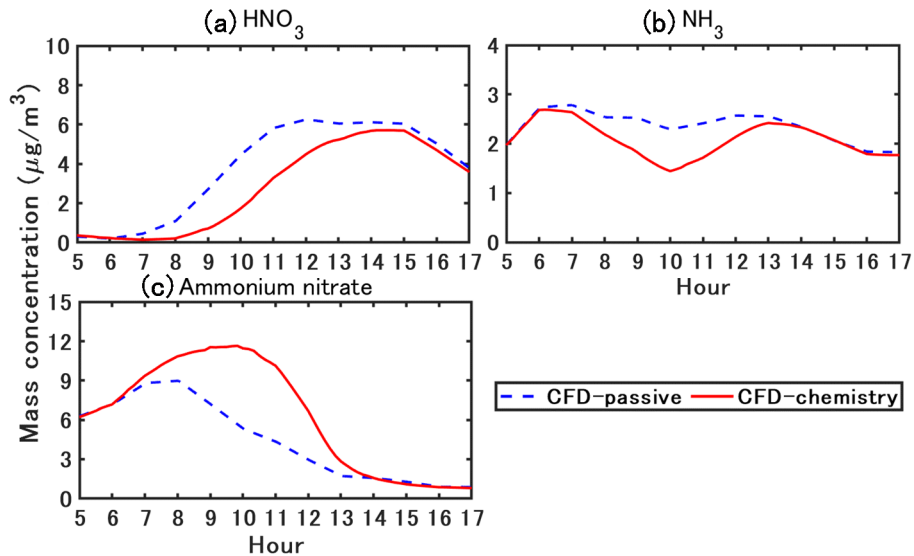
Fig. 14 Simulated time-varying concentrations of ammonium nitrate and precursor gas (HNO$_3$ and NH$_3$).

Fig. 14 shows the simulated time-varying concentrations of ammonium nitrate formed by the condensation of HNO$_3$ and NH$_3$. Based on the traffic fleet in the current study, NH$_3$ emission is approximately 1-2% of NOx emissions. Ammonium nitrate and HNO$_3$ are not emitted and differences between simulations with or without chemistry coupling are due to gas chemical reactions and phase change between the gas and particle. Phase change may be driven by NH$_3$ emissions, as well as the non-thermodynamic equilibrium of the background concentrations.

In CFD-passive, NH$_3$ concentration peaks around 7 a.m. as NOx because it is emitted by traffic. The peak in HNO$_3$ concentration is later in the morning, around 11 am. HNO$_3$ is formed from the oxidation of NO$_2$, which is emitted by traffic and is rapidly formed from NO traffic emissions. The formation of HNO$_3$ is slower than the formation of NO$_2$, and probably occurs at the regional scale, leading to a delay in the peak of HNO$_3$ concentration compared to NO$_2$ concentration. In CFD-chemistry, the temporal variations of HNO$_3$ concentration show large differences with CFD-passive because HNO$_3$ condenses with NH$_3$ to form ammonium nitrate during the daytime. As a result, the HNO$_3$ concentration peak in CFD-chemistry is later than that in CFD-passive (it is shifted from 11 a.m. to around 2 p.m.). The NH$_3$ concentration in CFD-passive peaks at 7 a.m. because of traffic emission and is stable from 7 a.m. to 1 p.m. and then decreases from 1 p.m. Meanwhile, the condensation in CFD-chemistry leads to lower concentration than in

513   CFD-passive during the daytime (between 7 a.m. and 1 p.m.).

514   For 12-hour time-averaged concentrations, ammonium nitrate increases by 46% in CFD-
515   chemistry compared with that in CFD-passive. Background ammonium nitrate
516   concentration (CFD-passive) peaks around the morning rush (7 to 8 a.m.) and then
517   decreases. Meanwhile, in CFD-chemistry, ammonium nitrate concentration peaks later
518   around 10 a.m., because of the large increase in HNO_3 between the traffic rush and 10
519   a.m. However, although HNO_3 concentration does not vary much between 11 a.m. and 3
520   p.m., the ammonium nitrate concentration decreases from 10 a.m. to a very small level
521   (lower than 1 $\mu g/m^3$) after 2 p.m. This decrease is probably linked to the temperature
522   increase during the daytime (Fig. 2(b)) and the relative humidity decrease, leading to a
523   decrease in the condensation rate (Stelson and Seinfeld, 1982).
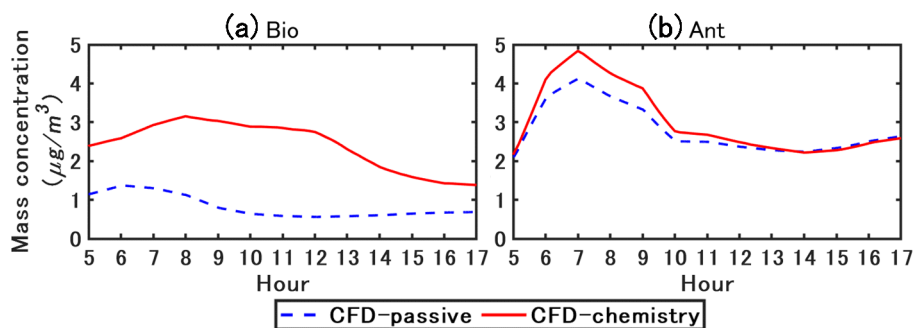
524

525   Fig. 15 Simulated time-varying concentration of organic matter. Bio refers to organic
526   matter formed from biogenic precursors. Ant refers to organic matter formed from
527   anthropogenic precursors.

528

529   Fig. 15 shows the simulated time-varying concentrations of organic matter. Organic
530   matter is divided into two main categories depending on the origin of the precursors: Bio
531   and Ant refer to the organic matter of biogenic and anthropogenic precursors respectively.
532   In CFD-chemistry, Bio concentration is larger than that in CFD-passive. As biogenic
533   precursors are not emitted in the street, the condensation of Bio is due to background
534   precursor gases. As discussed previously, the concentration of ammonium nitrate is higher
535   in CFD-chemistry than in CFD-passive, providing a larger aqueous mass onto which
536   hydrophilic compounds of the biogenic precursor gases condense. As the condensation of
537   ammonium nitrate decreases in the afternoon as shown in Fig. 14, the condensation of
538   Bio also decreases.

539   Ant is largely influenced by traffic emissions in the street, particularly by emissions of
540   semi-volatile compounds (Sartelet et al., 2018), which soon condenses after emissions.
541   Therefore there is a peak around 7 a.m. owing to the morning rush. In the model,
542   anthropogenic emissions are mostly hydrophobic, therefore the condensation is not

543 enhanced by the increase in inorganic concentrations. Consequently, the difference
544 between CFD-chemistry and CFD-passive is larger in the morning owing to the large
545 increase in traffic emissions, but small differences are observed in the afternoon.
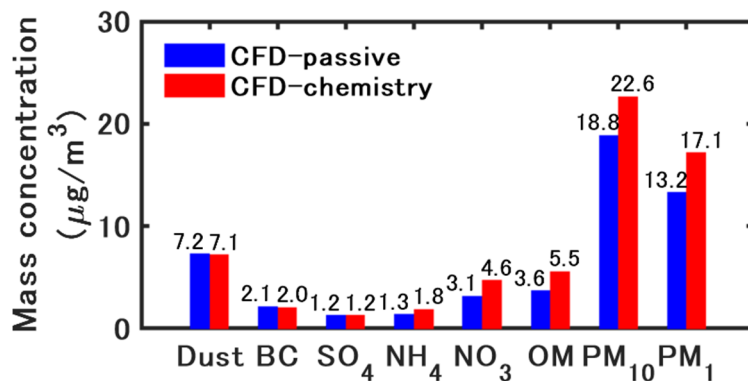
546
547 Fig. 16 Time-averaged concentration of PM_{10}, PM_1 and the chemical compounds of PM_{10}
548 from 5 a.m. to 5 p.m.
549
550 Fig. 16 shows the time-averaged concentrations of PM_{10}, PM_1 and the chemical
551 compounds of PM_{10} from 5 a.m. to 5 p.m. The time-averaged PM_{10} and PM_1
552 concentrations increase by approximately 3.8 $\mu g/m^3$ in CFD-chemistry compared to CFD-
553 passive, indicating that chemistry mainly influences small particles. Inert matter slightly
554 decreases in CFD-chemistry owing to dry deposition. Condensation increases of 48%,
555 38% and 53% of nitrate, ammonium and organic matter concentrations in CFD-chemistry
556 compared to CFD-passive.
557

558   *5.3. Size distribution of particle matter*

559
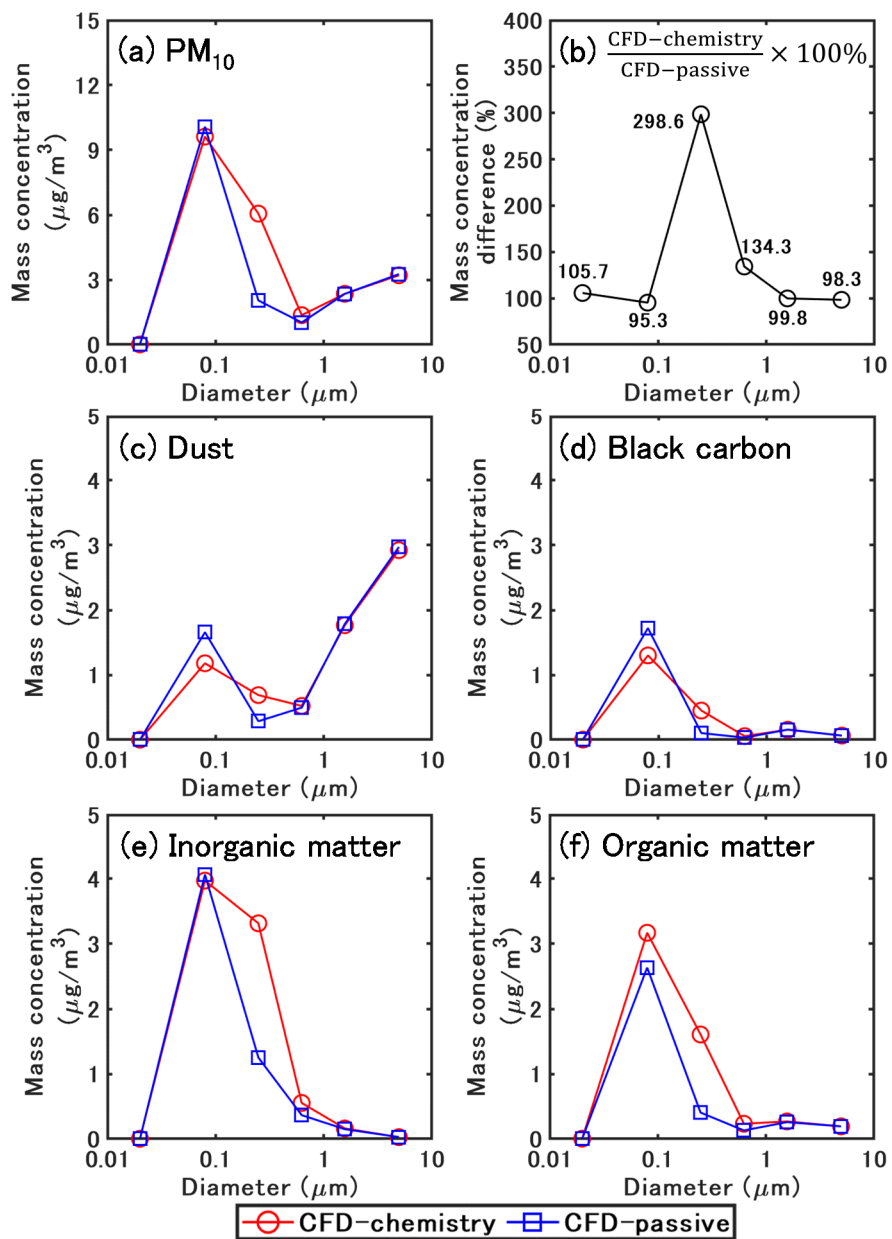
Fig. 17 Time-averaged size distribution of PM_{10} for different chemical species from 5 a.m. to 5 p.m.

562

Fig. 17 shows the time-averaged size distribution of PM_{10} for the different chemical compounds of particles from 5 a.m. to 5 p.m. The bound diameters are 0.01, 0.04, 0.16, 0.4, 1.0, 2.5 and 10 μm, and the mean diameters are 0.02, 0.08, 0.25, 0.63, 1.58 and 5.01 μm.

For the total concentration of PM_{10} (Fig. 17(a)), the lowest and the largest concentrations are in the first size section (0.01-0.04 μm) and the second size section (0.04-0.16 μm)

569   respectively, for both the CFD-passive and the CFD-chemistry simulations. Generally,
570   the loss and gain of mass concentration in each size section are related to emission, dry
571   deposition, coagulation (small particles coagulate into large particles), and
572   condensation/evaporation (phase exchange between gas and particles).
573   Fig. 17(b) shows the mass concentration ratio between CFD-passive and CFD-chemistry
574   for each size section. For particles in the size range of 0.04-0.16 μm, the concentrations
575   are smaller in CFD-chemistry than in CFD-passive, because dry deposition and
576   coagulation both decrease mass concentration for those particles. Furthermore, semi-
577   volatile gases may evaporate from small particles because of the Kelvin effect and
578   condense onto larger particles. For particles in the size range of 0.16-1.0 μm, the
579   concentrations are much larger in CFD-chemistry than CFD-passive, indicating that
580   coagulation and condensation on the mass-concentration increase are dominant to other
581   processes, such as deposition. For particles larger than 1 μm, the concentrations of CFD-
582   passive and CFD-chemistry are similar, because particle dynamics have a low influence
583   on large particles.
584   The size distribution of dust (Fig. 17(c)) shows that most dust mass concentrations are in
585   particles larger than 1 μm. Meanwhile, most of the mass concentration of BC, inorganic
586   and organic matter (Fig. 17(d-f)) is in particles smaller than 1 μm. Coagulation is the main
587   process influencing the size distribution for inert matter (dust and BC). Compared to
588   CFD-passive, the mass concentration of dust and BC in the second size section decrease
589   by 0.48 and 0.43 μg/m^3 in CFD-chemistry. Correspondingly, the mass concentrations of
590   dust and BC in the third size section increase by 0.41 and 0.35 μg/m^3.
591   For inorganic matter, in the second size section, the concentrations are similar in CFD-
592   passive and CFD-chemistry: particle dynamics decrease sulphate concentration by 0.32
593   μg/m^3 and increase nitrate concentration by 0.17 μg/m^3. However, as the results of the
594   combination effect of coagulation and ammonium nitrate condensation, the
595   concentrations largely increase in the third size section in CFD-chemistry: sulphate,
596   ammonium and nitrate increase by 0.27, 0.6 and 1.24 μg/m^3, respectively.
597   For organic matter, because of condensation of hydrophilic compounds from background
598   biogenic gases and anthropogenic emissions, CFD-chemistry leads to a small increase in
599   concentrations (0.53 μg/m^3) in the second size section and a large increase in the third
600   section (1.21 μg/m^3) compared to CFD-passive. In detail, Bio concentrations increase by
601   0.89 μg/m^3, and Ant concentrations decrease by 0.36 μg/m^3 in the second size section. In
602   the third size section, Bio and Ant concentrations increase by 0.67, 0.54 μg/m^3.
603

604   *5.4. Influence of ammonia traffic emissions*
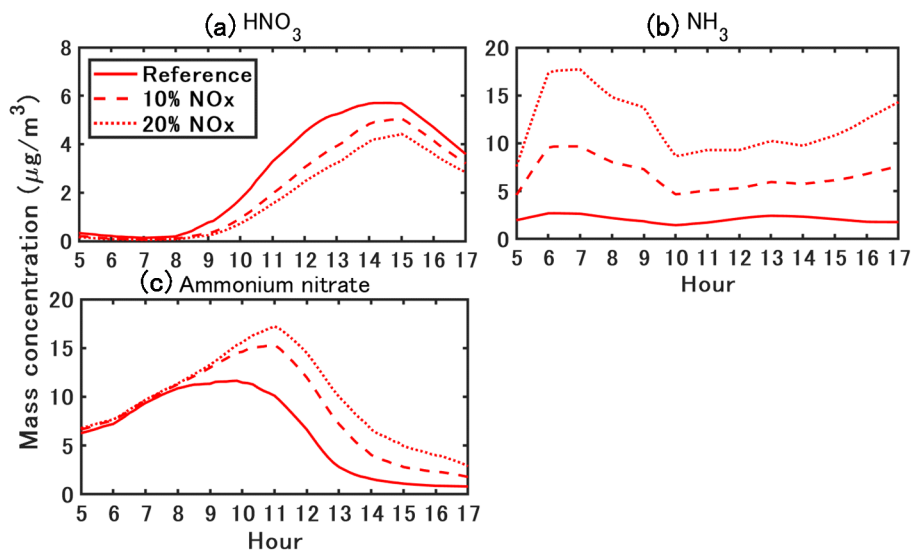
605

606   Fig. 18 Sensitivity of ammonium nitrate concentration to NH$_3$ emission.

607

608   Suarez-Bertoa et al. (2017) conducted on-road measurements of NH$_3$ emissions from two
609   Euro 6b compliant light duty cars (one gasoline and one diesel) under real-world driving
610   conditions, and they found that NH$_3$ emissions accounted for 11.9% and 0.92% of NOx
611   emissions for gasoline and diesel vehicles. As explained in Section 5.2, NH$_3$ emission
612   emissions are approximately 1-2% of NOx emissions in the reference case. Two cases are
613   considered to simulate the impact of an increase in the fraction of gasoline cars, and
614   sensitivity simulations are performed with NH$_3$ emission considered as 10% and 20% of
615   the NOx emissions.
616   Fig. 18 shows the sensitivity of ammonium nitrate concentration to NH$_3$ emissions. A
617   larger NH$_3$ emission delays the peak of ammonium nitrate by approximately one hour.
618   For a 12-hour average, considering NH$_3$ emissions of 10% and 20% of NOx emissions
619   leads to a large increase in ammonium nitrate (35% and 55%) compared to the reference
620   case, because of the formation of ammonium nitrate by the condensation of HNO$_3$ and
621   NH$_3$.

622

623   **6. Conclusions**
624   Particles in urban environment impose adverse impacts on pedestrians' health.
625   Conventional CFD methods regarding particles as passive scalars cannot reproduce the
626   formation of secondary aerosols and may lead to uncertain simulations. Therefore, to
627   increase the simulation accuracy of particle dispersion, we coupled the CFD software
628   OpenFOAM (OF) and Code_Saturne (CS) with SSH-Aerosol, a modular box model to

629 simulate the evolution of primary and secondary aerosols. The main processes involved
630 in the aerosol dynamics (coagulation, condensation /evaporation and dry deposition) were
631 considered.

632 We simulated a 12-hour transient dispersion of pollutants from traffic emissions in a street
633 canyon using the unsteady RANS model. The simulation domain was generated to model
634 a street-canyon where field measurements are available. The flow field was based on the
635 WRF model. The background concentrations of gas and particles were obtained from
636 regional-scale simulations with a chemistry-transport model. The particle diameter range
637 ($0.01\,\mu m$ to $10\,\mu m$) was divided into six size sections. The following conclusions were
638 drawn from the results of this study.

639 1) The simulated spatially-averaged values in the street canyon were validated from
640   field measurement using validation metrics. For both OF and CS, the simulated NO_2
641   and PM_{10} concentrations based on the coupling model (CFD-chemistry) achieved
642   better agreement with the measurement data than the conventional CFD simulation
643   which considered pollutants as passive scalars (CFD-passive). The differences
644   between of the OF and CS results were not obvious and were mainly due to the
645   differences in the turbulence scheme. The following conclusions were drawn based
646   on the simulated OF concentrations.

647 2) For the flow field, a large vortex was observed in the canyon with a small secondary
648   vortex at the corner of the leeward wall at the current aspect ratio (H/W=0.31). In
649   CFD-chemistry, because of the reverse flow, the 12-hour (from 5 a.m. to 5 p.m.) time-
650   averaged NO_2 mass concentration, PM_{10} mass and number concentrations at
651   pedestrian height were much higher near the leeward wall (116 $\mu g/m^3$, 28 $\mu g/m^3$,
652     $3.2 \times 10^{10}\,m^{-3}$) than the background (26 $\mu g/m^3$, 15 $\mu g/m^3$, $2.3 \times 10^{10}\,m^{-3}$).

653 3) Secondary aerosol formation largely affected the mass concentration and size
654   distribution of particle matter. For 12-hour time-averaged concentrations, ammonium
655   nitrate and organic matter increased by 46% and 53% in CFD-chemistry compared
656   to CFD-passive because of condensation of HNO_3 and NH_3, background biogenic
657   precursor-gases and anthropogenic precursor-gas emissions. Coagulation largely
658   influenced the size distribution of small particles by combining particles with a
659   diameter of 0.04-0.16 μm into 0.16-0.4 μm. At the same time, CFD-chemistry
660   showed a much larger concentration than CFD-passive for the particles in 0.16-1.0
661   μm, indicating that the effect of condensation on increasing mass concentration was
662   dominant compared to other chemical processes.

663 4) Urban areas are NH_3-limited (HNO_3 sufficient) areas, therefore, increasing NH_3 leads
664   to a large increase in ammonium nitrate. Vehicles are considered to be the main

665   source of NH_3 in urban environments. Increasing the fleet's proportion of recent
666   gasoline vehicles may increase NH_3 emissions. For a 12-hour average, we considered
667   NH_3 emissions of 10% and 20% of NOx emissions led to a large increase in
668   ammonium nitrate (35% and 55%) compared to the reference case which considers
669   NH_3 emission as 1-2% of NOx emissions.

670 5) A grid sensitivity analysis showed that the particles' concentrations of inorganic and
671   organic compounds were sensitive to grid resolution, whereas inert particle
672   concentrations were not sensitive to grid resolution. In addition, simulated values
673   based on a grid size of 0.5 m in the street canyon showed small differences with a
674   grid size of 0.25 m, indicating that a spatial resolution of 0.5 m can be enough for
675   reactive particle dispersion at the street level.

676 6) Operator splitting is often employed to solve the transport term and chemical
677   reactions over a given time step in chemical transport simulations. Two integration
678   orders were considered: A-B splitting method (CFD(Δt)-Chemistry(Δt)) and A-B-A
679   splitting method (CFD($\Delta t/2$)-Chemistry(Δt)-CFD($\Delta t/2$)). The results showed that
680   the A-B-A splitting method had almost the same concentrations as the A-B splitting
681   method with half the computational time. Further sensitivity analysis on the time step
682   showed that a time step of 0.5 s was enough when using the A-B-A splitting method.

683 7) Conducting a CFD simulation with constant boundary conditions and emission rates
684   at a specific time point is considered a practical method to achieve time-averaged
685   concentrations for evaluating street-level pollutant concentrations. The validation
686   was conducted using conditions on five time points (7 a.m., 10 a.m., 1 p.m., 3 p.m.
687   and 5 p.m.). The simulated concentration based on the above method exhibited
688   almost the same value as the simulation with transient conditions at the same time
689   points.

690 The limitation of this study should be addressed as several reasonable approximations
691 and assumptions were made in the simulation settings.

692 1) Concerning the simulation domain: since we focused on the coupling of gas chemical
693   reactions and particle dynamics to the CFD codes, we selected a 12-hour period when
694   wind direction was perpendicular to the street. In that case, a 2-D simplification of
695   the simulation domain is reasonable, as shown by Maison et al. (2022). In addition,
696   the 2-D simplification is frequently adopted for studying dispersion of reactive
697   pollutants in a street canyon (Garmory et al., 2009; Wu et al., 2021). However, in
698   more general cases, the pollutant residence time for a 3-D canyon could be shorter
699   compared to the 2-D canyon adopted in this study, and the effects of chemical
700   reaction or aerosol processes could be weaker than this study reported. In addition,

701   various wind directions should be considered to better evaluate the performance of
702   the coupled model. Further work will focus on the application of the coupled model
703   to a complex urban environment with changing wind directions.
704 2) Concerning the physical model: the simulations were based on RANS-closure, and
705   the SSH-aerosol processed the ensemble-averaged concentration, therefore the
706   covariance of turbulent diffusion and chemical reaction may not be fully reproduced.
707   The simulation based on LES may provide better prediction of second-order
708   quantities. In addition, the radiation on the wall may lead street-level-variations of
709   temperature and could affect the flow field and chemical reaction rates. However,
710   this was not considered here, and the radiation effect on the local temperature was
711   simplified as being the same as in the inflow condition. The inflow temperature was
712   obtained from WRF model where the radiation was considered, and the time variation
713   of temperature was considered to be the same as the background.
714 Future work will be conducted on the influence of environmental factors and emission
715 conditions, aiming to provide knowledge to devise suitable countermeasures to decrease
716 particle concentration in microscale urban environments.
717

718 Acknowledgments: This work benefited from discussions with Bertrand Carissimo. The
719 authors acknowledge funding from DIM QI^2 (Air Quality Research Network on air
720 quality in the Île-de-France region) and from Île-de-France region.

721

722 Code/Data availability
723 The codes used in this publication are available to the community, and they can be
724 accessed by request to the corresponding author.
725

726 Author contribution
727 KS and RO were responsible for conceptualization. CL, YW, CF, KS, YK and ZW
728 developed the software. CL and YW conduced the visualization and validation; CL, YW
729 and KS performed the formal analysis. KS and RO acquired resources. CL, YW, RO and
730 KS were responsible for writing and original draft preparation. CF, YK, HK reviewed and
731 edited the manuscript All co-authors contributed to the discussion of the paper.
732

733 Competing interests
734 The contact author has declared that neither they nor their co-authors have any
735 competing interests.
736

737   Reference

738   Anenberg, S. C., Miller, J., Minjares, R., Du, L., Henze, D. K., Lacey, F., Malley, C. S.,

739   Emberson, L., Franco, V., Klimont, Z., and Heyes, C.: Impacts and mitigation of excess

740   diesel-related NO x emissions in 11 major vehicle markets, Nature, 545, 467–471,

741   https://doi.org/10.1038/nature22086, 2017.

742   EMEP/EEA: EMEP/EEA air pollutant emission inventory guidebook 2019, EEA Report

743   No 13/2019, European Environment Agency:

744   https://www.eea.europa.eu/publications/emep-eea-guidebook-2019, last access: 14

745   March 2022.

746   Archambeau, F., Méchitoua, N., and Sakiz, M.: Code Saturne: A Finite Volume Code for

747   Turbulent flows - Industrial Applications, International Journal on Finite Volumes, 1,

748   2004.

749   Arpaci, V. S. and Larsen, P. S.: Convection Heat Transfer, Prentice Hall, New York,

750   1984.

751   Belcher, S. E.: Mixing and transport in urban areas, Philosophical Transactions of the

752   Royal Society A: Mathematical, Physical and Engineering Sciences, 363, 2947–2968,

753   https://doi.org/10.1098/rsta.2005.1673, 2005.

754   Bishop, G. A. and Stedman, D. H.: Reactive Nitrogen Species Emission Trends in Three

755   Light-/Medium-Duty United States Fleets, Environ Sci Technol, 49, 11234–11240,

756   https://doi.org/10.1021/acs.est.5b02392, 2015.

757   Blackman, K., Perret, L., and Savory, E.: Effect of upstream flow regime on street

758   canyon flow mean turbulence statistics, Environmental Fluid Mechanics, 15, 823–849,

759   https://doi.org/10.1007/s10652-014-9386-8, 2015.

760   Blocken, B., Tominaga, Y., and Stathopoulos, T.: CFD simulation of micro-scale

761   pollutant dispersion in the built environment, Build Environ, 64, 225–230,

762   https://doi.org/10.1016/j.buildenv.2013.01.001, 2013.

763   Boutahar, J., Lacour, S., Mallet, V., Quelo, D., Roustan, Y., and Sportisse, B.:

764   Development and validation of a fully modular platform for numerical modelling of air

765   pollution: POLAIR, Int J Environ Pollut, 22, 17,

766   https://doi.org/10.1504/IJEP.2004.005474, 2004.

767   Chang, J. C. and Hanna, S. R.: Air quality model performance evaluation, Meteorology

768   and Atmospheric Physics, 87, 167–196, https://doi.org/10.1007/s00703-003-0070-7,

769   2004.

770   Du, Y., Xu, X., Chu, M., Guo, Y., and Wang, J.: Air particulate matter and

771   cardiovascular disease: The epidemiological, biomedical and clinical evidence,

772   https://doi.org/10.3978/j.issn.2072-1439.2015.11.37, 2016.

773 Ferrero, E., Alessandrini, S., Anderson, B., Tomasi, E., Jimenez, P., and Meech, S.:

774 Lagrangian simulation of smoke plume from fire and validation using ground-based

775 lidar and aircraft measurements, Atmos Environ, 213, 659–674,

776 https://doi.org/10.1016/j.atmosenv.2019.06.049, 2019.

777 Fu, K. and Liang, D.: The conservative characteristic FD methods for atmospheric

778 aerosol transport problems, J Comput Phys, 305, 494–520,

779 https://doi.org/10.1016/j.jcp.2015.10.049, 2016.

780 Gao, S., Kurppa, M., Chan, C. K., and Ngan, K.: Technical note: Dispersion of cooking-

781 generated aerosols from an urban street canyon, Atmos Chem Phys, 22, 2703–2726,

782 https://doi.org/10.5194/acp-22-2703-2022, 2022.

783 Guimet, V. and Laurence, D.: A linearised turbulent production in the k-ε model for

784 engineering applications, in: Engineering Turbulence Modelling and Experiments 5,

785 edited by: Rodi, W. and Fueyo, N., Elsevier Science Ltd, Oxford, UK, 157–166, 2002.

786 Hanna, S. R., Hansen, O. R., and Dharmavaram, S.: FLACS CFD air quality model

787 performance evaluation with Kit Fox, MUST, Prairie Grass, and EMU observations,

788 Atmos Environ, 38, 4675–4687, https://doi.org/10.1016/j.atmosenv.2004.05.041, 2004.

789 Harten, A.: On a Class of High Resolution Total-Variation-Stable Finite-Difference

790 Schemes, SIAM J Numer Anal, 21, 1–23, https://doi.org/10.1137/0721001, 1984.

791 Jones, A. M., Yin, J., and Harrison, R. M.: The weekday–weekend difference and the

792 estimation of the non-vehicle contributions to the urban increment of airborne

793 particulate matter, Atmos Environ, 42, 4467–4479,

794 https://doi.org/10.1016/j.atmosenv.2008.02.001, 2008.

795 Kim, M. J.: Sensitivity of nitrate aerosol production to vehicular emissions in an urban

796 street, Atmosphere (Basel), 10, 212, https://doi.org/10.3390/ATMOS10040212, 2019.

797 Kim, M. J., Park, R. J., Kim, J. J., Park, S. H., Chang, L. S., Lee, D. G., and Choi, J. Y.:

798 Computational fluid dynamics simulation of reactive fine particulate matter in a street

799 canyon, Atmos Environ, 209, 54–66, https://doi.org/10.1016/j.atmosenv.2019.04.013,

800 2019.

801 Kim, Y., Wu, Y., Seigneur, C., and Roustan, Y.: Multi-scale modeling of urban air

802 pollution: development and application of a Street-in-Grid model (v1.0) by coupling

803 MUNICH (v1.0) and Polair3D (v1.8.1), Geosci Model Dev, 11, 611–629,

804 https://doi.org/10.5194/gmd-11-611-2018, 2018.

805 Kim, Y., Lugon, L., Maison, A., Sarica, T., Roustan, Y., Valari, M., Zhang, Y., André,

806 M., Sartelet, K., Paris-saclay, U., and Ecosys, U. M. R.: MUNICH v2.0: A street-

807 network model coupled with SSH-aerosol (v1.2) for multi-pollutant modelling, Geosci

808 Model Dev, 15, 7371-7396, https://doi.org/10.5194/gmd-15-7371-2022, 2022.

809   Kumar, P., Fennell, P., Langley, D., and Britter, R.: Pseudo-simultaneous measurements

810   for the vertical variation of coarse, fine and ultrafine particles in an urban street canyon,

811   Atmos Environ, 42, 4304–4319, https://doi.org/10.1016/j.atmosenv.2008.01.010, 2008.

812   Kurppa, M., Hellsten, A., Roldin, P., Kokkola, H., Tonttila, J., Auvinen, M., Kent, C.,

813   Kumar, P., Maronga, B., and Järvi, L.: Implementation of the sectional aerosol module

814   SALSA2.0 into the PALM model system 6.0: Model development and first evaluation,

815   Geosci Model Dev, 12, 1403–1422, https://doi.org/10.5194/gmd-12-1403-2019, 2019.

816   Lo, K. W. and Ngan, K.: Characterising the pollutant ventilation characteristics of street

817   canyons using the tracer age and age spectrum, Atmos Environ, 122, 611–621,

818   https://doi.org/10.1016/j.atmosenv.2015.10.023, 2015.

819   Lo, K. W. and Ngan, K.: Characterizing ventilation and exposure in street canyons using

820   Lagrangian particles, J Appl Meteorol Climatol, 56, 1177–1194,

821   https://doi.org/10.1175/JAMC-D-16-0168.1, 2017.

822   Lugon, L., Vigneron, J., Debert, C., Chrétien, O., and Sartelet, K.: Black carbon

823   modeling in urban areas: investigating the influence of resuspension and non-exhaust

824   emissions in streets using the Street-in-Grid model for inert particles (SinG-inert),

825   Geosci Model Dev, 14, 7001–7019, https://doi.org/10.5194/gmd-14-7001-2021, 2021a.

826   Lugon, L., Sartelet, K., Kim, Y., Vigneron, J., and Chretien, O.: Simulation of primary

827   and secondary particles in the streets of Paris using MUNICH, Faraday Discuss, 226,

828   432–456, https://doi.org/10.1039/d0fd00092b, 2021b.

829   Maison, A., Flageul, C., Carissimo, B., Wang, Y., Tuzet, A., and Sartelet, K.:

830   Parameterizing the aerodynamic effect of trees in street canyons for the street network

831   model MUNICH using the CFD model Code_Saturne, Atmos Chem Phys, 22, 9369–

832   9388, https://doi.org/10.5194/acp-22-9369-2022, 2022.

833   OpenFOAM user guide: https://www.openfoam.com/.

834   Parente, A., Gorlé, C., van Beeck, J., and Benocci, C.: Improved k–ε model and wall

835   function formulation for the RANS simulation of ABL flows, Journal of Wind

836   Engineering and Industrial Aerodynamics, 99, 267–278,

837   https://doi.org/10.1016/j.jweia.2010.12.017, 2011.

838   Di Sabatino, S., Buccolieri, R., Pulvirenti, B., and Britter, R.: Simulations of pollutant

839   dispersion within idealised urban-type geometries with CFD and integral models, Atmos

840   Environ, 41, 8316–8329, https://doi.org/10.1016/j.atmosenv.2007.06.052, 2007.

841   Sartelet, K., Zhu, S., Moukhtar, S., André, M., André, J. M., Gros, V., Favez, O.,

842   Brasseur, A., and Redaelli, M.: Emission of intermediate, semi and low volatile organic

843   compounds from traffic and their impact on secondary organic aerosol concentrations

844   over Greater Paris, Atmos Environ, 180, 126–137,

845   https://doi.org/10.1016/j.atmosenv.2018.02.031, 2018.

846   Sartelet, K., Couvidat, F., Wang, Z., Flageul, C., and Kim, Y.: SSH-aerosol v1.1: A

847   modular box model to simulate the evolution of primary and secondary aerosols,

848   Atmosphere (Basel), 11, 525, https://doi.org/10.3390/atmos11050525, 2020.

849   Sartelet, K. N., Debry, E., Fahey, K., Roustan, Y., Tombette, M., and Sportisse, B.:

850   Simulation of aerosols and gas-phase species over Europe with the Polyphemus system:

851   Part I-Model-to-data comparison for 2001, Atmos Environ, 41, 6116–6131,

852   https://doi.org/10.1016/j.atmosenv.2007.04.024, 2007.

853   Sportisse, B.: An Analysis of Operator Splitting Techniques in the Stiff Case, J Comput

854   Phys, 161, 140–168, https://doi.org/10.1006/jcph.2000.6495, 2000.

855   Stelson, A. W. and Seinfeld, J. H.: Relative humidity and temperature dependence of the

856   ammonium nitrate dissociation constant, Atmospheric Environment (1967), 16, 983–

857   992, https://doi.org/10.1016/0004-6981(82)90184-6, 1982.

858   Suarez-Bertoa, R. and Astorga, C.: Impact of cold temperature on Euro 6 passenger car

859   emissions, Environmental Pollution, 234, 318–329,

860   https://doi.org/10.1016/j.envpol.2017.10.096, 2018.

861   Suarez-Bertoa, R., Mendoza-Villafuerte, P., Riccobono, F., Vojtisek, M., Pechout, M.,

862   Perujo, A., and Astorga, C.: On-road measurement of NH 3 emissions from gasoline and

863   diesel passenger cars during real world driving conditions, Atmos Environ, 166, 488–

864   497, https://doi.org/10.1016/j.atmosenv.2017.07.056, 2017.

865   Sun, K., Tao, L., Miller, D. J., Pan, D., Golston, L. M., Zondlo, M. A., Griffin, R. J.,

866   Wallace, H. W., Leong, Y. J., Yang, M. M., Zhang, Y., Mauzerall, D. L., and Zhu, T.:

867   Vehicle Emissions as an Important Urban Ammonia Source in the United States and

868   China, Environ Sci Technol, 51, 2472–2481, https://doi.org/10.1021/acs.est.6b02805,

869   2017.

870   Sung, J. C., Pulliam, B. L., and Edwards, D. A.: Nanoparticles for drug delivery to the

871   lungs, Trends Biotechnol, 25, 563–570, https://doi.org/10.1016/j.tibtech.2007.09.005,

872   2007.

873   Tominaga, Y. and Stathopoulos, T.: Turbulent Schmidt numbers for CFD analysis with

874   various types of flowfield, Atmos Environ, 41, 8091–8099,

875   https://doi.org/10.1016/j.atmosenv.2007.06.054, 2007.

876   Tominaga, Y. and Stathopoulos, T.: CFD simulation of near-field pollutant dispersion in

877   the urban environment: A review of current modeling techniques, Atmos Environ, 79,

878   716–730, https://doi.org/10.1016/j.atmosenv.2013.07.028, 2013.

879   Trini Castelli, S., Armand, P., Tinarelli, G., Duchenne, C., and Nibart, M.: Validation of

880   a Lagrangian particle dispersion model with wind tunnel and field experiments in urban

881   environment, Atmos Environ, 193, 273–289,

882   https://doi.org/10.1016/j.atmosenv.2018.08.045, 2018.

883   Wesely, M. L.: Parameterization of surface resistances to gaseous dry deposition in

884   regional-scale numerical models, Atmospheric Environment (1967), 23, 1293–1304,

885   https://doi.org/10.1016/0004-6981(89)90153-4, 1989.

886   Wu, L., Hang, J., Wang, X., Shao, M., and Gong, C.: APFoam 1.0: Integrated

887   computational fluid dynamics simulation of O3-NOx-volatile organic compound

888   chemistry and pollutant dispersion in a typical street canyon, Geosci Model Dev, 14,

889   4655–4681, https://doi.org/10.5194/gmd-14-4655-2021, 2021.

890   Yakhot, V., Orszag, S. A., Thangam, S., Gatski, T. B., and Speziale, C. G.: Development

891   of turbulence models for shear flows by a double expansion technique, Physics of Fluids

892   A, 4, 1510–1520, https://doi.org/10.1063/1.858424, 1992.

893   Yee, H. C.: Construction of explicit and implicit symmetric TVD schemes and their

894   applications, J Comput Phys, 68, 151–179, https://doi.org/10.1016/0021-

895   9991(87)90049-0, 1987.

896   Zhang, K., Chen, G., Zhang, Y., Liu, S., Wang, X., Wang, B., and Hang, J.: Integrated

897   impacts of turbulent mixing and NOX-O3 photochemistry on reactive pollutant

898   dispersion and intake fraction in shallow and deep street canyons, Science of The Total

899   Environment, 712, 135553, https://doi.org/10.1016/j.scitotenv.2019.135553, 2020.

900   Zhang, L., Gong, S., Padro, J., and Barrie, L.: A size-segregated particle dry deposition

901   scheme for an atmospheric aerosol module, Atmos Environ, 35, 549–560,

902   https://doi.org/10.1016/S1352-2310(00)00326-5, 2001.

903   Zhang, L., Brook, J. R., and Vet, R.: A revised parameterization for gaseous dry

904   deposition in air-quality models, Atmos Chem Phys, 3, 2067–2082,

905   https://doi.org/10.5194/acp-3-2067-2003, 2003.

906

907   Appendix A

908   The schemes for particle deposition velocity v_d were added to the transport equations

909   using volume sink terms based on (Zhang et al., 2001) and can be represented as:

$$v_{d,p} = \begin{cases} v_g + \dfrac{1}{R_a + R_s}, & \text{Wall surfaces} \\ v_g, & \text{Entire field} \end{cases} \qquad (A1)$$

$$v_g = \frac{\rho d_p^2 g C}{18 \eta} \qquad (A2)$$

$$R_a = \frac{\text{In}(z_R/z_0) - \psi_H}{\kappa u_*} \tag{A3}$$

$$R_s = \frac{1}{\varepsilon_0 u_* (E_B + E_{IM} + E_{IN}) R_1} \tag{A4}$$

910 The deposition velocity for the particles $v_{d,p}$ consists of both gravitational settling and
911 surface deposition near the wall surfaces. The gravitational settling velocity v_g was
912 considered for the entire field, ρ is the particle density; d_p is the particle diameter; g
913 is the acceleration of gravity; C is Cunningham correction factor for small particles; η
914 is the viscosity coefficient of air.
915 The aerodynamic resistance R_a is calculated from the first-layer-height z_R, roughness
916 length z_0, Von Kármán constant κ, friction velocity u_* and stability function ψ_H. For the
917 k–ε model, u_* is estimated by $\left(C_\mu^{0.5} k\right)^{0.5}$ and $C_\mu = 0.09$ is a constant of the model.
918 The surface resistance R_s is calculated from u_*, the collection efficiency from Brownian
919 diffusion E_B, the impaction E_{IM} and the interception E_{IN}. The correction factor
920 represents the fraction of particles that stick to the surface R_1 and an empirical
921 constant $\varepsilon_0 = 3$.
922 The dry deposition schemes for gas were added to the transport equations using volume
923 sink terms based on (Wesely, 1989) and (Zhang et al., 2003),which can be represented as:

$$v_{d,g} = \frac{1}{R_a + R_b + R_c} \tag{A5}$$

$$R_b = \frac{2}{\kappa u_*} \left(\frac{Sc}{Pr}\right)^{2/3} \tag{A6}$$

924 The deposition velocity for gas $v_{d,g}$ is calculated from the aerodynamic resistance R_a,
925 the quasi-laminar layer resistance R_b and the surface resistance for gas R_c. $Sc = v/D$
926 and $Pr = 0.72$ are the Schmidt and Prandtl number. v is the kinematic viscosity of air
927 and D is the molecular diffusivity of different gases. R_c is calculated based on (Zhang
928 et al., 2003).
929

930 Appendix B
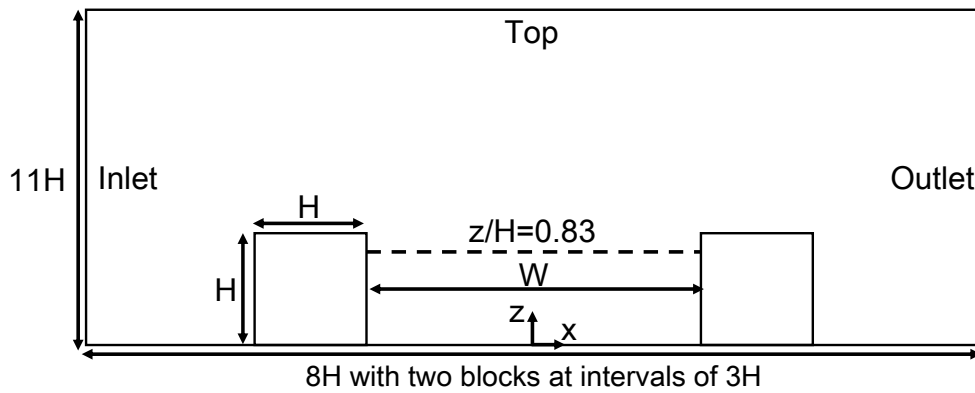
931

932 Fig. B1 Simulation domain for velocity validation.

933

934 Correctly representing the flow field in the street canyon is important to model accurately
935 the concentrations. Unfortunately, observation data on wind velocity is the street is not
936 available. Therefore, we conducted a velocity validation for OpenFOAM v2012 using
937 data from a wind tunnel experiment (Blackman et al., 2015). The 2-D simulation domain
938 is shown in Fig. B1. The aspect ratio in the experiment (H/W=0.33) is close to this study
939 (H/W=0.31). The building height H is 0.06 m. The grid size is 1/20 H in x- and z-
940 directions in the simulation domain under $3H$. The free-stream velocity U_{ref} is 5.9 m/s.
941 The steady-state flow field is simulated with the same turbulence model (RNG k–ε model)
942 as in the paper, and cyclic boundary conditions are used for the inlet and outlet. The slip
943 boundary is considered for the top, and non-slip boundary conditions with the same wall
944 functions as in the paper are considered for other walls.
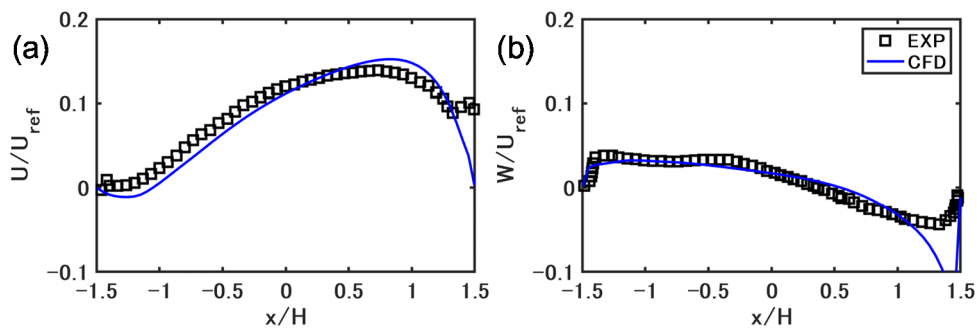
945

946 Fig. B2 Streamwise and vertical direction of mean wind velocities at $z/H = 0.83$.

947

948 Fig. B2 compares the simulated streamwise and vertical direction of mean wind velocities
949 with the experimental values at $z/H = 0.83$. The RNG k–ε model reproduce well the
950 velocities, although the velocities very close to the windward wall show differences with

951 the experimental values. The above validation shows that if suitable inlet conditions are
952 given, the flow field is well reproduced with the turbulence model adopted in this study.